Electronic supplementary materials

For https://doi.org/10.1631/jzus.A2200427

Molecular force mechanism of hydrodynamics in clay nanopores

Shengjie WEI, Yuchao LI✉, Peng SHEN, Yunmin CHEN

MOE Key Laboratory of Soft Soils and Geoenvironmental Engineering, College of Civil Engineering and Architecture, Zhejiang University, Hangzhou 310058, China

✉ Yuchao LI, liyuchao@zju.edu.cn

Note S1 Number Density Profiles

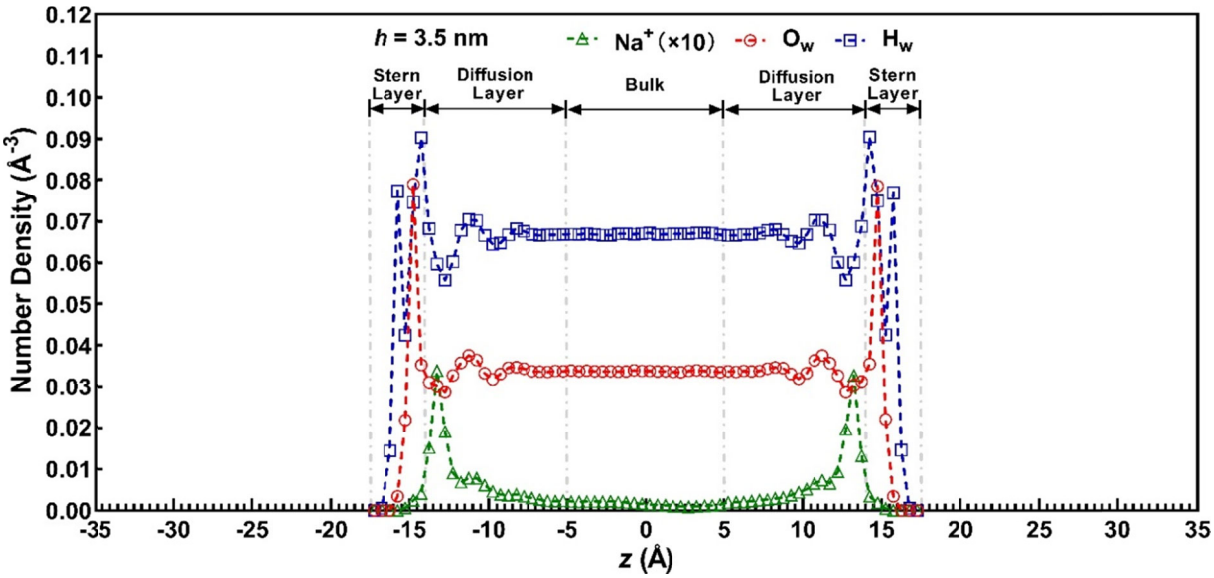

(a) h = 3.5 nm

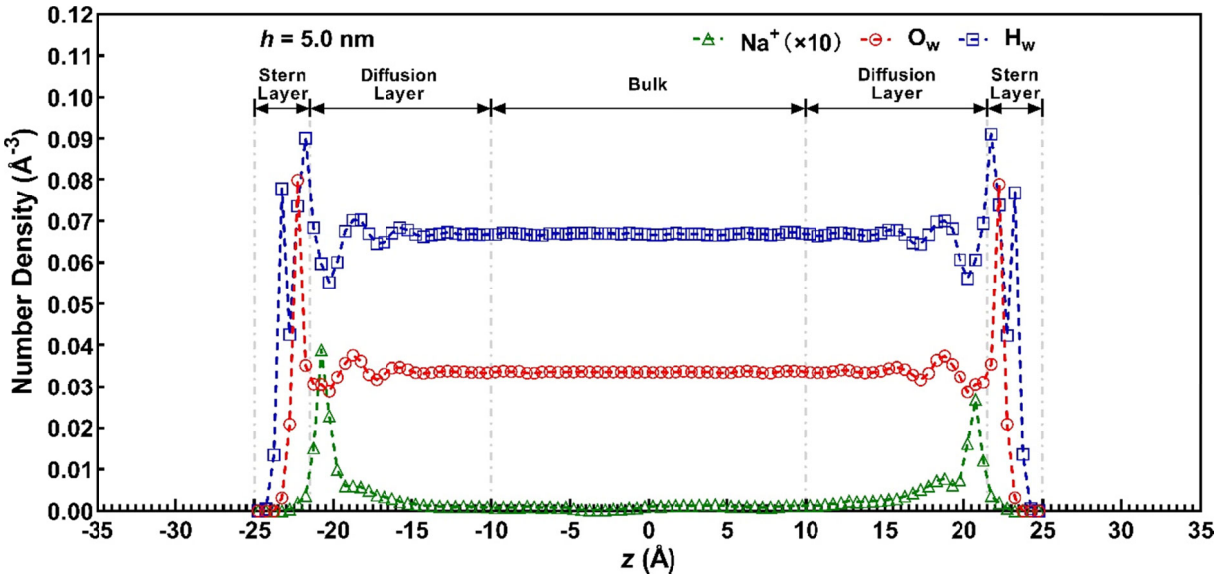

(b) h = 5.0 nm

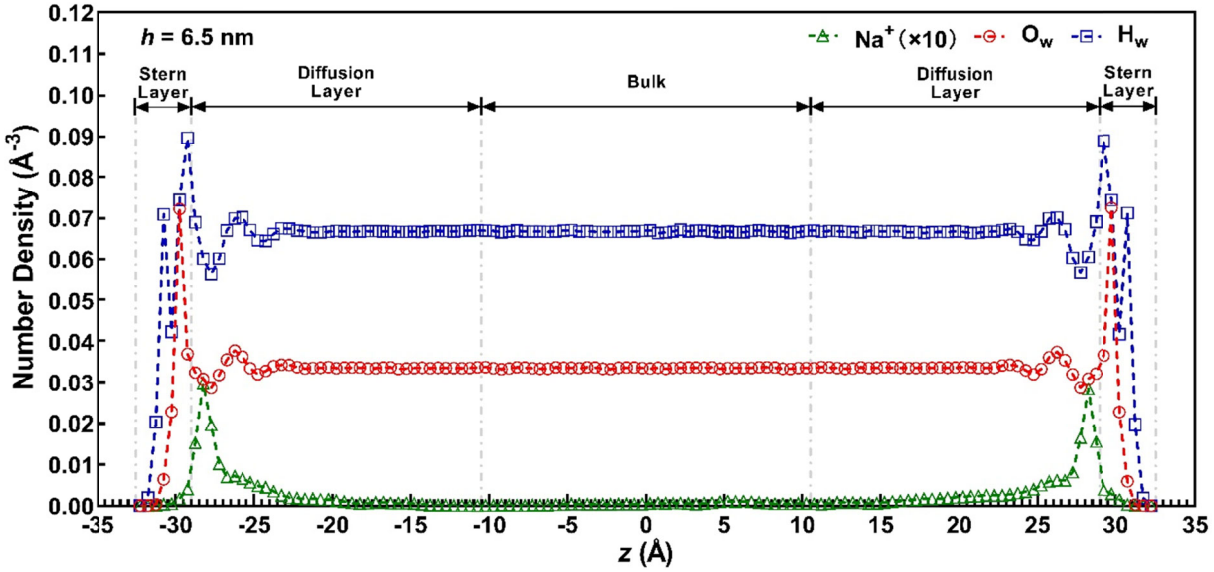

(c) h = 6.5 nm

Fig. S1 Number density of water oxygen atoms, water hydrogen atoms and cations

Note S2 Velocity Profiles for h = 5.0 and 6.5 nm

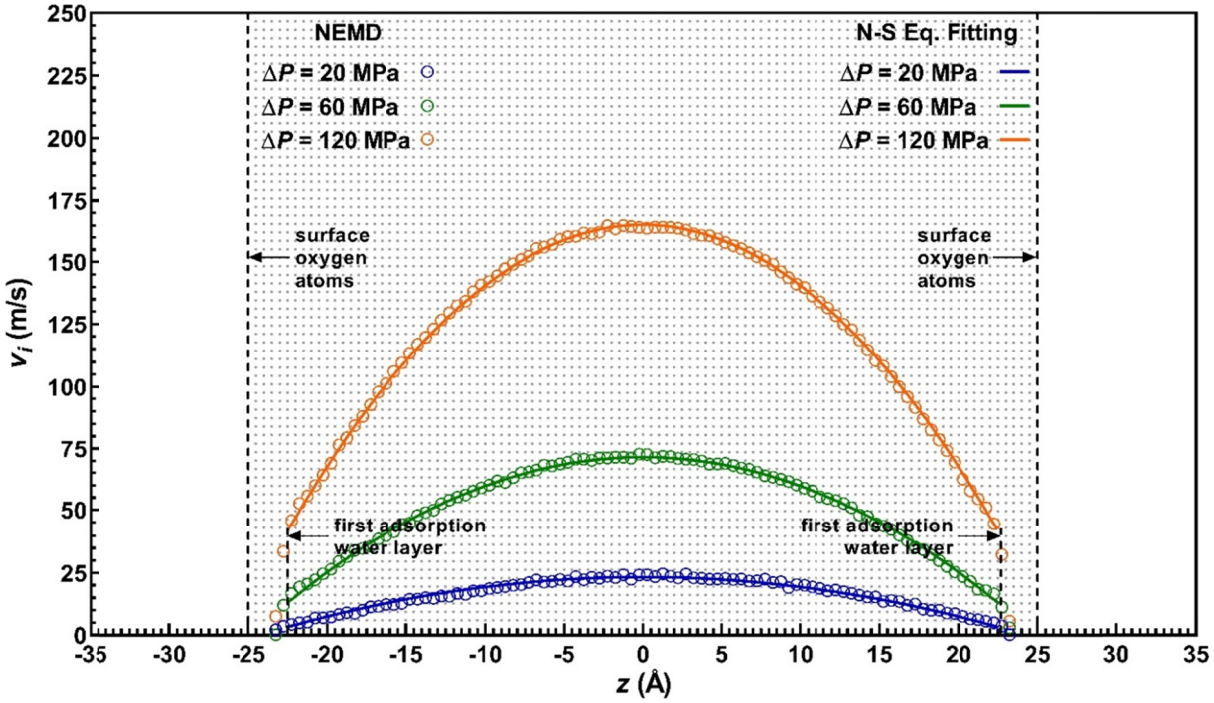

(a) h = 5.0 nm

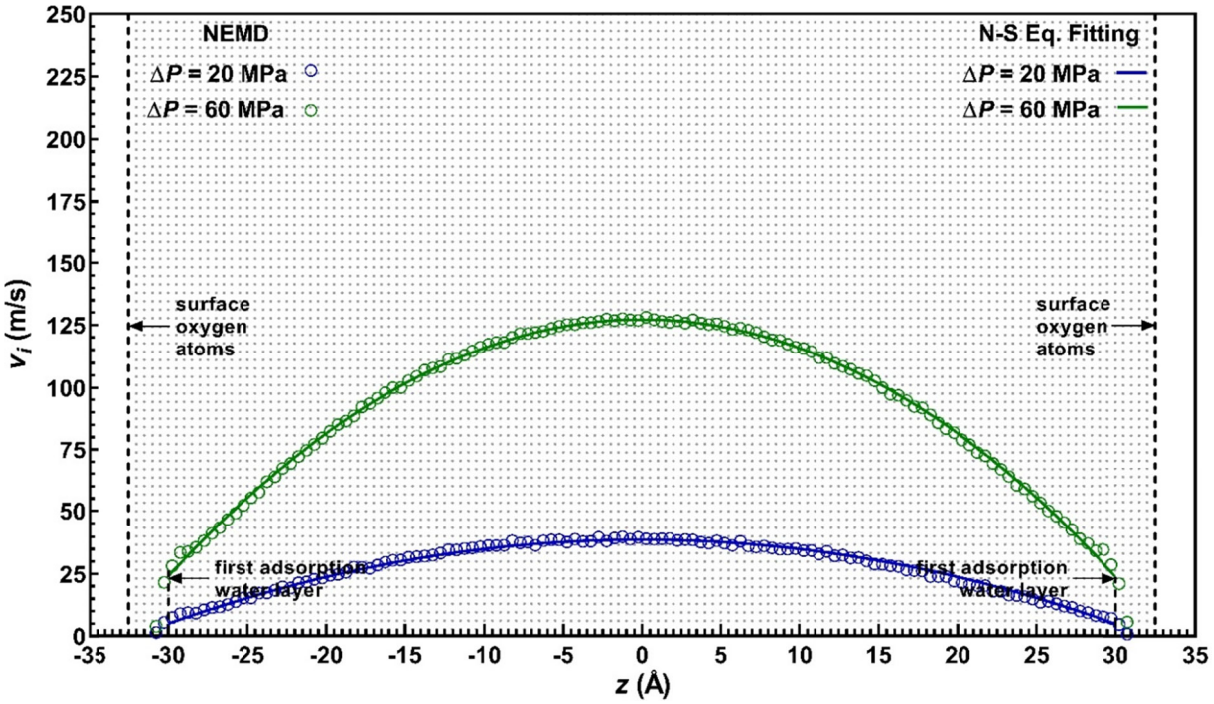

(b) h = 6.5 nm

Fig. S2 Velocity profiles of water flow in clay nanopores with h = 5.0 and 6.5 nm

Note S3 Green-Kubo Method and Contributions of Different Stress Parts

The shear viscosity $\eta_{\alpha\beta}$ can be calculated via the Green-Kubo formula (Kondratyuk N, 2019):

$$\eta_{\alpha\beta} = \frac{V}{k_B T}\int_0^{\infty}\left\langle \sigma_{\alpha\beta}(0)\sigma_{\alpha\beta}(t)\right\rangle \mathrm{d}t \tag{S1}$$

where V is the volume of bulk water, k_B is the Boltzmann constant (k_B = 1.380649×10-23 J/K), T = 300 K is the temperature, $\sigma_{\alpha\beta}(t)$ is the off-diagonal component of stress tensor and the notation '< >' stands for an average over the canonical ensemble. The shear viscosity η is the average of η_{xy}, η_{xz} and η_{yz}. The stress tensor $\sigma_{\alpha\beta}$ is defined as the virial stress and calculated as follows:

$$\sigma_{\alpha\beta}V = \sum_{i=1}^{N} m_i v_{i\alpha} v_{i\beta} + \sum_{i=1}^{N} r_{i\alpha} f_{i\beta} \tag{S2}$$

where N is the number of atoms, $r_{i\alpha}$ and $v_{i\alpha}$ are the α-components of coordinate and velocity of the i^{th} atom and $f_{i\alpha}$ is the α-component of force acting on the i^{th} atom. The calculation results are plotted in Fig. S3:

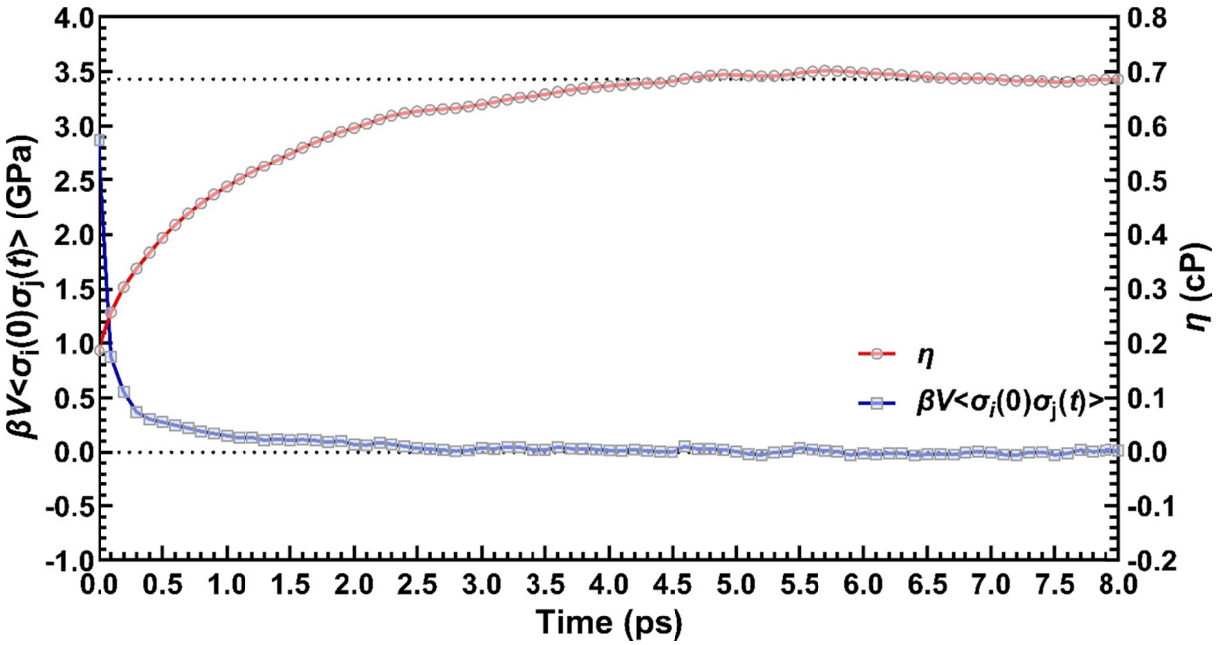

Fig. S3 The variation curve of the auto-correlation function of off-diagonal stress tensor (blue) and the accumulation curve of the viscosity of bulk water (red)

Obviously, as the simulation proceeds, the auto-correlation function (ACF) of the off-diagonal component of stress tensor gradually decays to zero and the integral of ACF over 8 ps shows that the viscosity of water in SPC/E model is about 0.69 cP. It is slightly smaller than the results (0.71±0.05 cP) by NEMD simulations in this paper and agrees with the results in other related work (Sami Tazi et al., 2012).

To figure out how different parts of the stress tensor contribute to the shear viscosity integral, the cross-terms produced by the kinetic, Coulomb and van der Waals parts of stress tensor are calculated (the contributions from bond stretching and angle bending are neglectable in the rigid water model). The results are illustrated by the hear map with 9 cells:

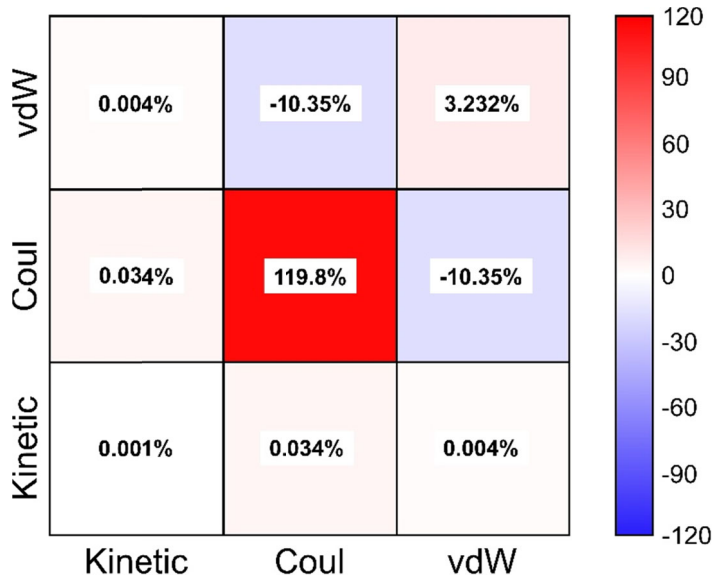

Fig. S4 The contributions to the Green-Kubo viscosity integral of different stress tensor parts of bulk water

It is found that the highest positive value of the integral contributions is the Coul-Coul (119.8%) part. The off-diagonal value $<\sigma_{\alpha\beta}^{Coul}(0)\ \sigma_{\alpha\beta}^{vdW}(t)>$ (-10.35%) indicates that the Coulomb electrostatic force and van der Waals force pose different influences on the viscosity, which causes negative correlation.

Note S4 Outflow Volume

To make a comparison with the flow velocity calculated by averaging the velocity profiles along the z-axis, another calculation method for average flow velocity is introduced, annotated as v_2. Due to the periodic condition, the model theoretically has an infinite-long flow path in y-direction, and the outflow water molecules at $y = L_y$ are also the inflow water molecules at $y = 0$ in the next timestep. Therefore, we collect the unwrapped coordinates of water molecules during the sampling time to calculate the real displacements of them in y-direction. If the real displacement Δy of the water molecule satisfies $n \cdot L_y \leq \Delta y < (n+1) \cdot L_y$ (n is an integer), it implies that the water molecule has flowed through the whole pore volume in the simulation box for n times, which is equivalent of the situation that n water molecules have flowed through the pore volume in the simulation box for once. Under this premise, we can calculate the number of water molecules that have flowed through the pore volume in the simulation box at every timestep during the sampling time and treat them as bulk water with the mass density of 0.997 g/cm^3, therefore, the outflow volume per area can also be determined, as shown in Fig. S3.

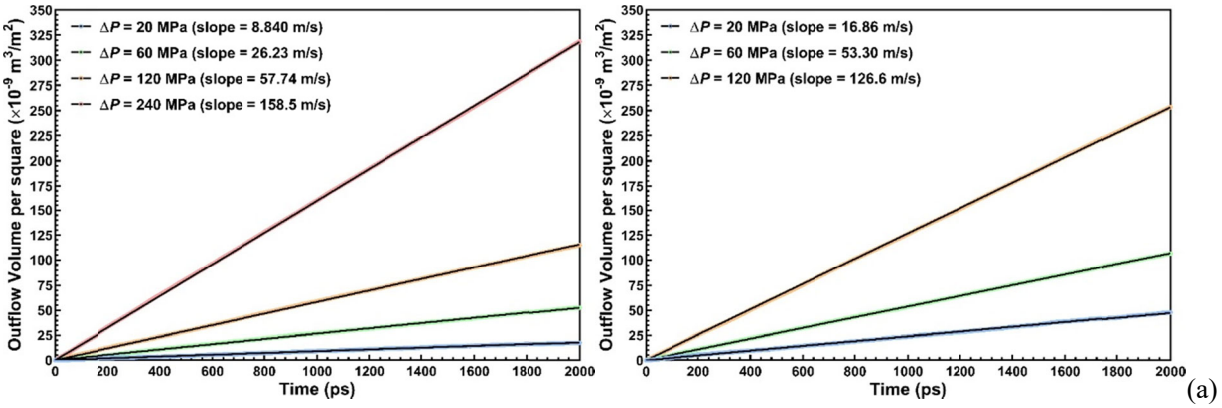

(a) h = 3.5 nm (b) h = 5.0 nm

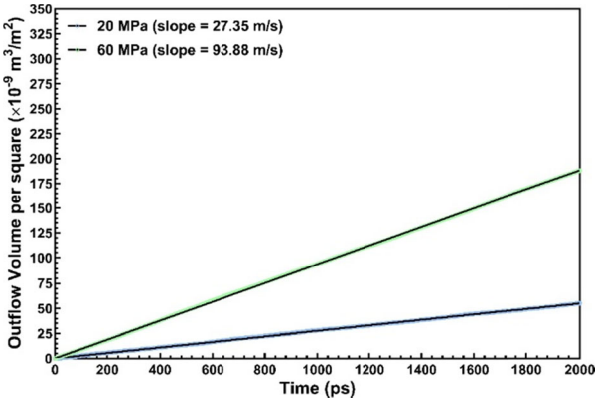

(c) h = 6.5 nm

Fig. S5 The variation curves with time of the outflow volume per unit area

According to Fig. S5, the outflow volume per unit area grows linearly with time and the growth rate (i.e., slope of the fitting line) is the average flow velocity v_2:

$$v_2 = \frac{Q}{L_x h t} \tag{S3}$$

As the applied flow-driving force increases, the average flow velocity increases as well.

Note S5 Water Structure and Arrangement in Stern Layer

S5.1 Planar Distribution

There are significant differences between the bulk water molecules and the water molecules in the Stern

Layer, therefore further statistical analyses are conducted for the planar distribution of water molecules in the Stern Layer (distance away from the mineral surface is around 1 ~ 4 Å). We divide the Stern Layer into six laminas with width of 0.5 Å and calculate the distribution probability of water hydrogen atom and water oxygen atom in the middle four laminas respectively, as shown in Fig. S6.

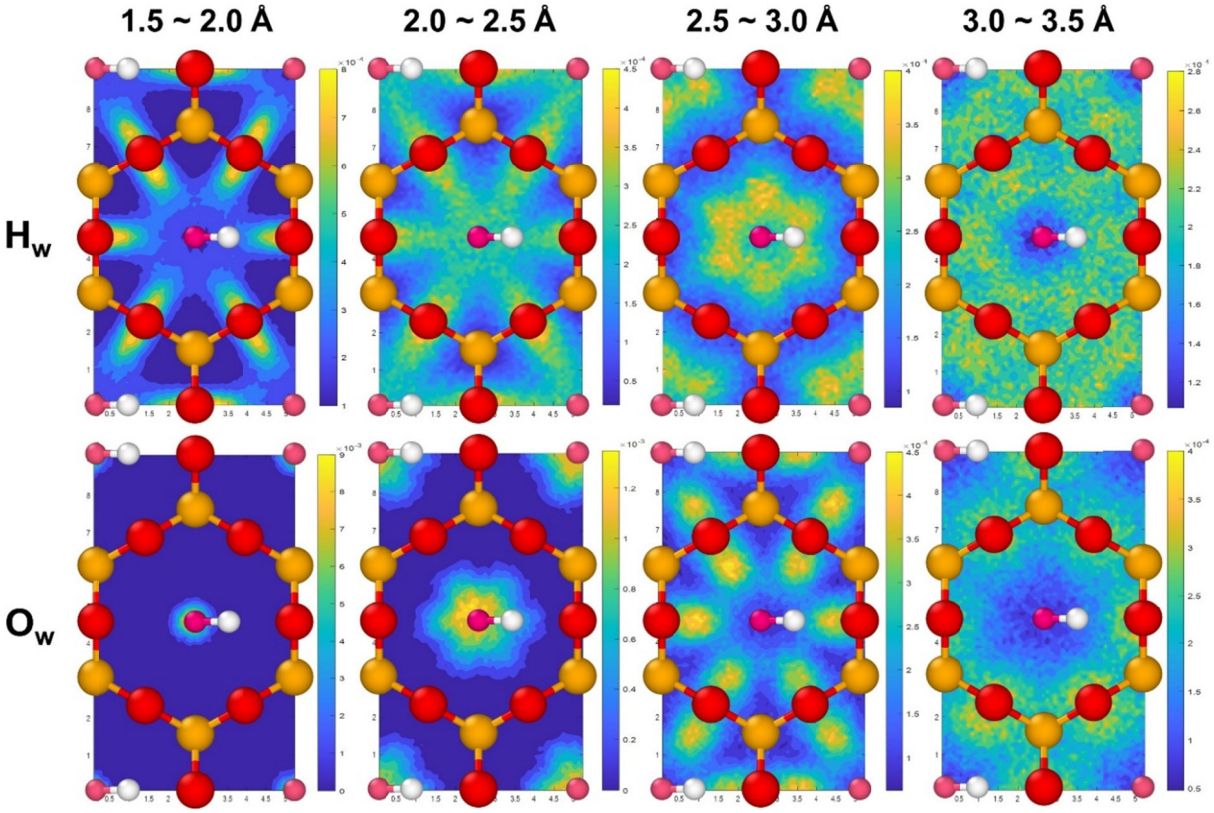

Fig. S6 The cloud map of plane distribution of water molecules in Stern Layer in unit cell. Yellow stands for high distribution probability while blue stands for low distribution probability

According to density profiles of water molecules (Fig. 2), the first density peak of water hydrogen atom is beneath 2.5 Å from the mineral surface and the other density peak of water hydrogen atom is more than 2.5 Å from the mineral surface. Hence, the planar distributions of water hydrogen atoms and water oxygen atoms are completely different before and after 2.5 Å from the surface. Due to the electrostatic attraction, the first hydrogen atom of water molecule has a clear propensity to reside over surface bridging oxygen atoms and avoid being above the silicon atoms (Marry et al., 2008), as shown in the first image on the top row of Fig. S4. At this time, the hydrogen atom is easy to form the hydrogen bond with bridging oxygen atoms and averagely there are 2.1 water molecules above a unit cell of the clay mineral that have formed

the hydrogen bonds with surface oxygen atoms. Within this range, the water oxygen atoms keep away from the bridging oxygen atoms because of van der Waals repulsion and prefer the sites in the cavity center (see the first image on the bottom row of Fig. S6). As the distance from the clay mineral surface increases and the van der Waals repulsion decays, the planar distribution of water oxygen atoms spread to the sites near the bridging oxygen atoms from the center of cavity (see the second image on the bottom row of Fig. S6).

The second hydrogen atoms of water molecules are annularly distributed around the center of the hexagonal cavity (see the third image on the top row of Fig. S6) under the O-H bond-interaction between the second water hydrogen atoms and the water oxygen atoms below, which reside in the center of cavity as mentioned above. The water oxygen atoms at this height prefer sites near (but not above) the bridging oxygen atoms (see the third image on the bottom row of Fig. S6).

As shown in Fig. S6, the water oxygen atoms within the range of 2.5 ~ 3 Å from the clay crystal layers locate near (but not above) the bridging oxygen atoms and the average coordinates of them in each area are close to the centroid of the area (Table S1).

Table S1 Average plane coordinates of water oxygen atoms in each area and the coordinates of the centroid of the area.

Area	Average coordinates of O_w		Centroid of the zone	
	X (Å)	Y (Å)	X (Å)	Y (Å)
I	1.775±0.018	6.111±0.058	1.760	6.093
II	3.496±0.011	6.122±0.054	3.520	6.093
III	0.885±0.017	4.622±0.072	0.880	4.570
IV	4.411±0.003	4.618±0.067	4.400	4.570
V	1.732±0.060	3.067±0.008	1.760	3.047
VI	3.548±0.065	3.049±0.021	3.520	3.047

S5.2 Morphology

The morphology of water molecule was described by three characteristic angles in this paper: (1) orientation angle α between the orientation vector of water molecule $\vec{\mu}$ and the positive direction of the z-axis; (2) interplanar angle β between the normal vector $\vec{n}$ of the plane where the water molecule locates

and the positive direction of the *z*-axis; (3) rotation angle γ between the projection of the orientation vector $\vec{\mu}$ on the *x*-*y* plane and the positive direction of *x*-axis. The schematic diagrams are illustrated in Fig. S7:

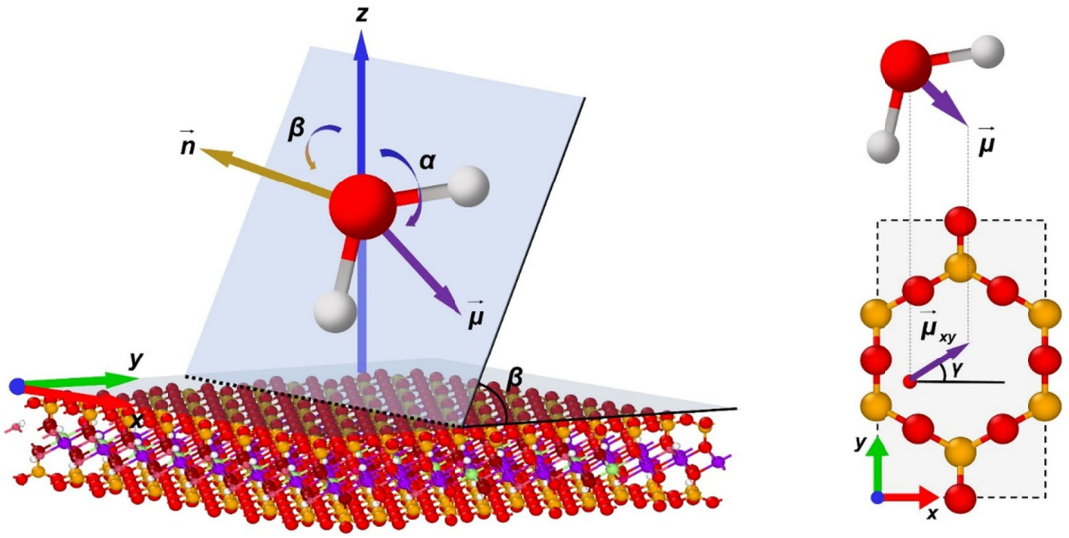

(a) Angles α and β (b) Angle γ

Fig. S7 Schematic diagram of three characteristic angles of water molecules

The distribution profiles of characteristic angles α and β are calculated, as shown in Fig. S8. The results indicate that different pore sizes and various applied flow-driving forces have slight influence on the distribution profiles of angles α and β along the *z*-axis.

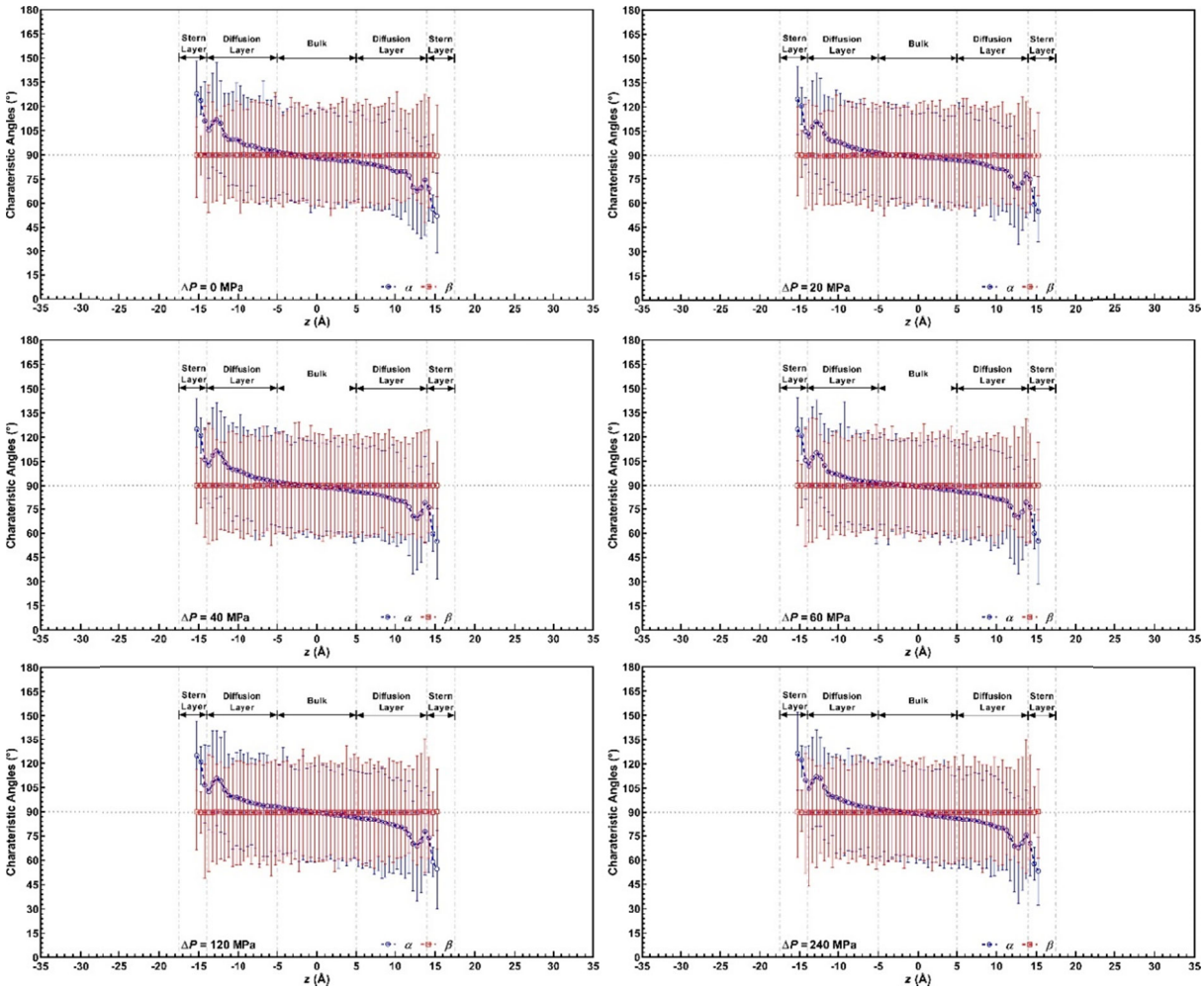
Stern Layer
Diffusion Layer
Bulk
Diffusion Layer
Stern Layer
Charateristic Angles (°)
z (Å)
ΔP = 0 MPa
ΔP = 20 MPa
ΔP = 40 MPa
ΔP = 60 MPa
ΔP = 120 MPa
ΔP = 240 MPa
α
β

(a) $h = 3.5$ nm

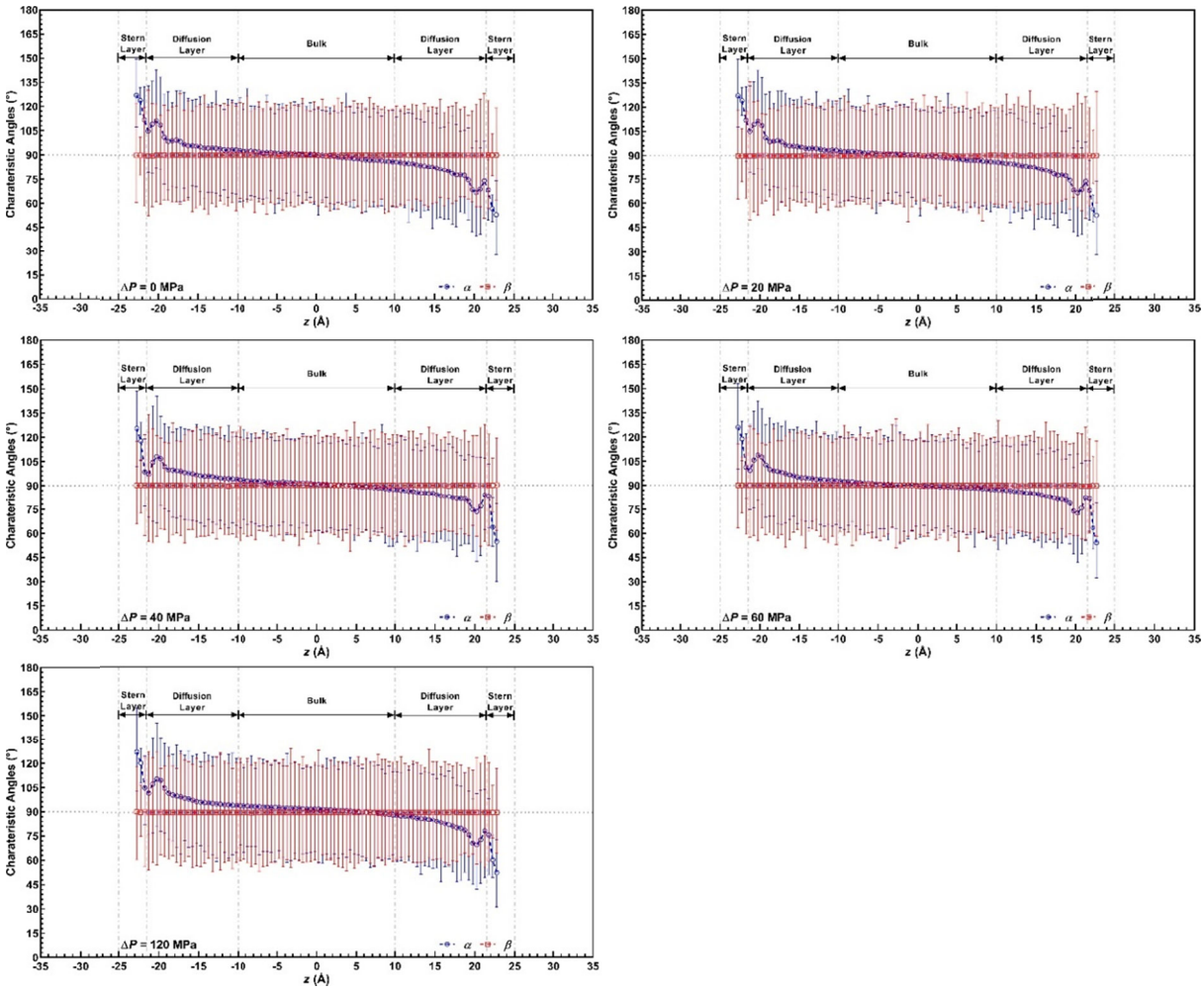

(b) h = 5.0 nm

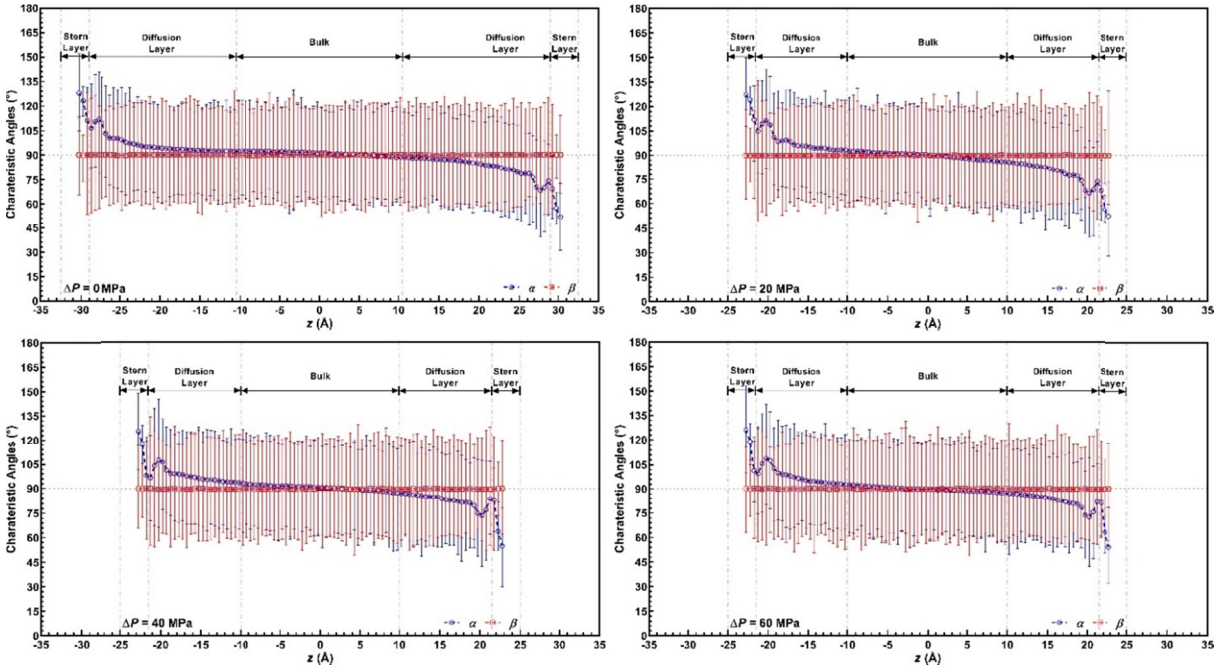

(c) h = 6.5 nm

Fig. S8 Profiles of characteristic angles of α and β

The distribution profiles of α and β along the z-axis for h = 3.5 nm are taken as an example. The orientation angle α represents the degree of polarization of water molecule and its distribution profile is anti-symmetric about the center of the pore. As the distance away from the lower clay mineral surface increases, the average orientation angle α approximately decreases from 128° to 90° and the degree of polarization gradually recedes. In the Stern Layer, the degree of polarization is greatly affected by the clay crystal layers, thus, the angle α has a dominant reduction from 128° to 102°. In the Diffusion Layer, the degree of polarization of water molecules first increases then decreases due to the influence of cations. In the Bulk Region, the degree of polarization slowly decreases as the increase of the distance from the clay mineral surface. The distribution profile of the planar angle β remains constant along the z-axis and the average value of β approximately equals 90°, indicating that angle β is independent of the location of water molecules and it is evenly distributed between 60° and 120°.

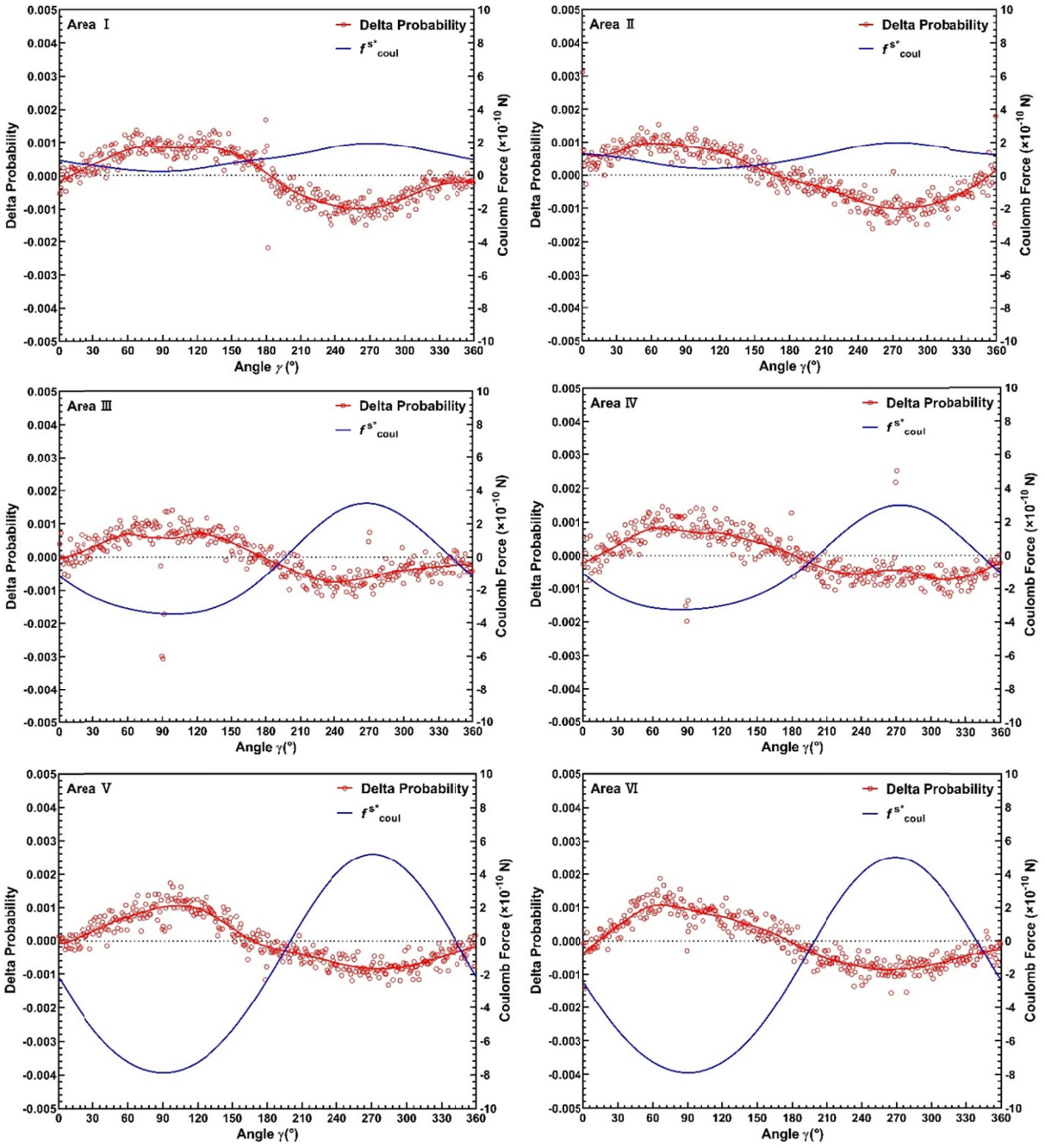

Fig. S9 Electrostatic forces on a single water molecule and probability differences between ΔP = 240 MPa and ΔP = 0 MPa for water molecules with different rotation angles γ

Note S6 Forces profiles of f^{s}, f^{s}_{vdW} and f^{s}_{Coul}

The 3.5-nm width clay nanopore is considered as the study case and the distributed force of clay crystal layers on water molecules f^{s} under different equivalent flow-driving pressures ΔP, as shown in Fig. S10.

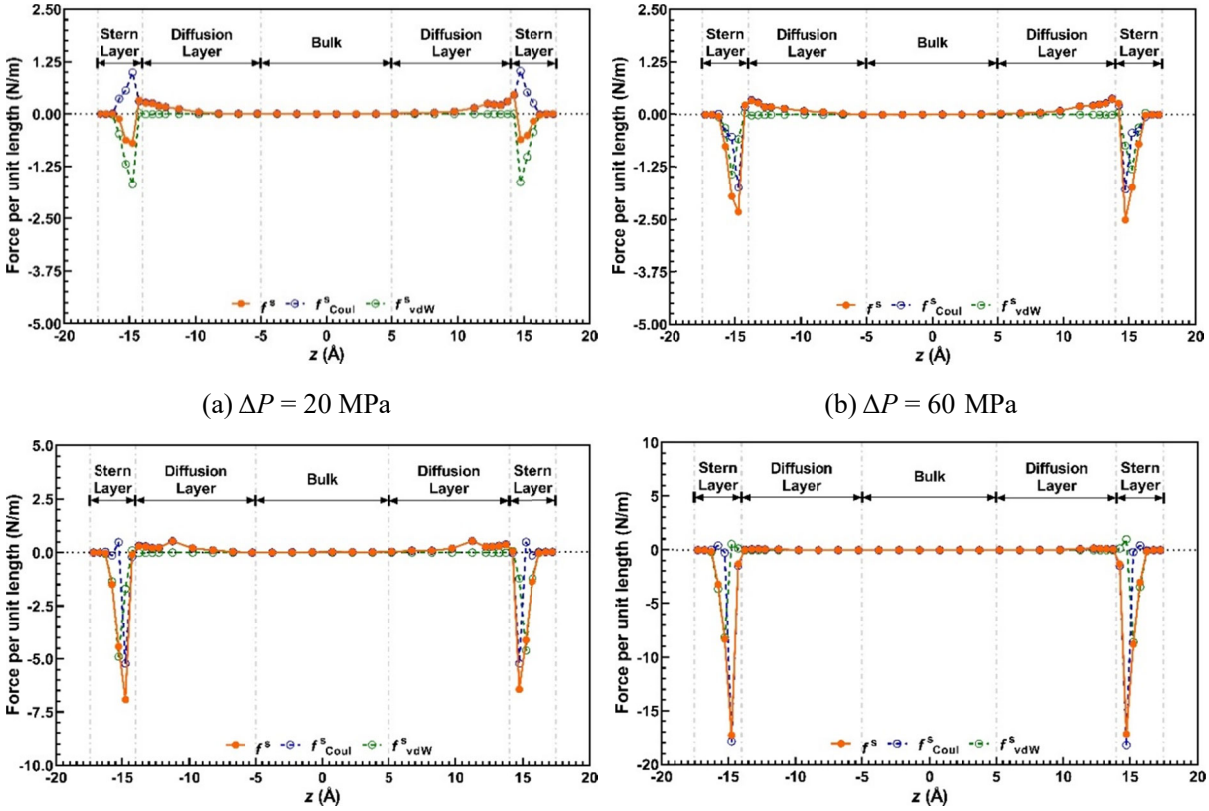

(a) ΔP = 20 MPa (b) ΔP = 60 MPa

(c) ΔP = 120 MPa (d) ΔP = 240 MPa

Fig. S10 Forces profiles of f^s (orange), f^s_{vdW} (green) and f^s_{Coul} (blue) along the *z*-axis

As shown in Fig. S10, f^s is symmetric about the center of the nanopore and it concentrates within the range of 1 ~ 4 Å away from the clay mineral surface (i.e., the Stern Layer). The peak of the force occurs at around 2.5 ~ 3 Å away from the mineral surface, and the peak values of the resistant force are -0.69 (-0.61), -2.33 (-2.53), -6.92 (-6.44) and -17.30 (-17.18) N/m for ΔP = 20, 60, 120 and 240 MPa respectively. The values ahead of the brackets represent the force on the water molecules near the left clay mineral surface and the values inside the brackets represent the force on water molecules closer to the right clay mineral surface (Fig. 1).

The f^s consists of the short-range van der Waals component f^s_{vdW} and long-range Coulomb electrostatic component f^s_{Coul}. f^s_{vdW} is a resistant force and the peak of it occurs at around 2 ~ 2.5 Å from the clay mineral surface, which is slightly closer to the surface than the peak of f^s. As the driving pressure increases, the resistant f^s_{vdW} becomes stronger and the peak values of it are -1.69(-1.64), -1.43 (-1.31), -4.90 (-4.61) and -8.19 (-8.63) N/m respectively. When the driving pressure is relatively low ($\Delta P \leq$ 20 MPa), the f^s_{Coul} is an

attractive force. However, once the resistant f^{s}_{vdW} fails to balance the increasing applied flow-driving force (ΔP > 20 MPa), the f^{s}_{Coul} turns to be a resistant force and gradually plays a leading role in f^{s}. The peak of it occurs around 2.5 ~ 3 Å from the clay mineral surface, which is slightly farther than the peak of f^{s}_{vdW}. The peak values of f^{s}_{Coul} are 0.99 (1.03), -1.75 (-1.79), -5.23 (-5.22) and -17.86 (-18.21) N/m for ΔP = 20, 60, 120 and 240 MPa respectively.

Note S7 Profiles of f^{w}, f^{w}_{vdW} and f^{w}_{Coul}

To explore the distribution differences along the *z*-axis of f^{w} as well as its van der Waals component f^{w}_{vdW} and Coulomb electrostatic component f^{w}_{Coul}, the profiles of f^{w}, f^{w}_{vdW} and f^{w}_{Coul} under ΔP = 240 MPa are plotted in Fig. S11.

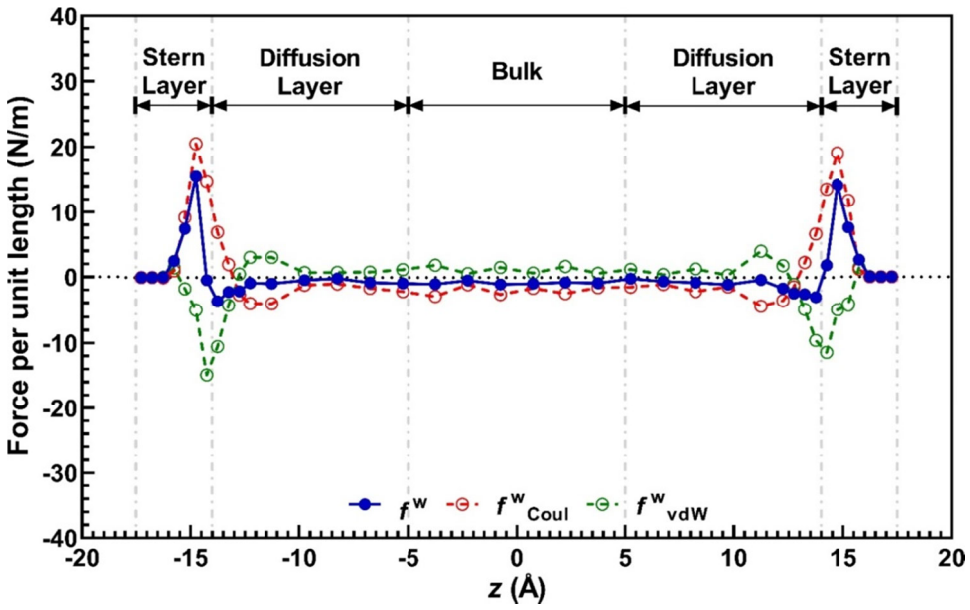

Fig. S11 Profiles of f^{w} (blue), f^{w}_{vdW} (red), and f^{w}_{Coul} (green) along the *z*-axis

As the pressure increases, the random thermal motions become relatively inapparent and thus, the variation modes of f^{w}, f^{w}_{vdW} and f^{w}_{Coul} gradually become clear. f^{w}_{vdW} and f^{w}_{Coul} have opposite signs and f^{w}_{Coul} takes the leading role in f^{w}. In the Stern Layer, f^{w} and f^{w}_{Coul} have a significant increment due to the force of the clay crystal layers. With the increase of the distance from clay mineral surface, f^{w} and f^{w}_{Coul} gradually increase after the sharp decrease in the Diffusion Layer.

Note S8 XY-Planar Distribution of Forces from FL

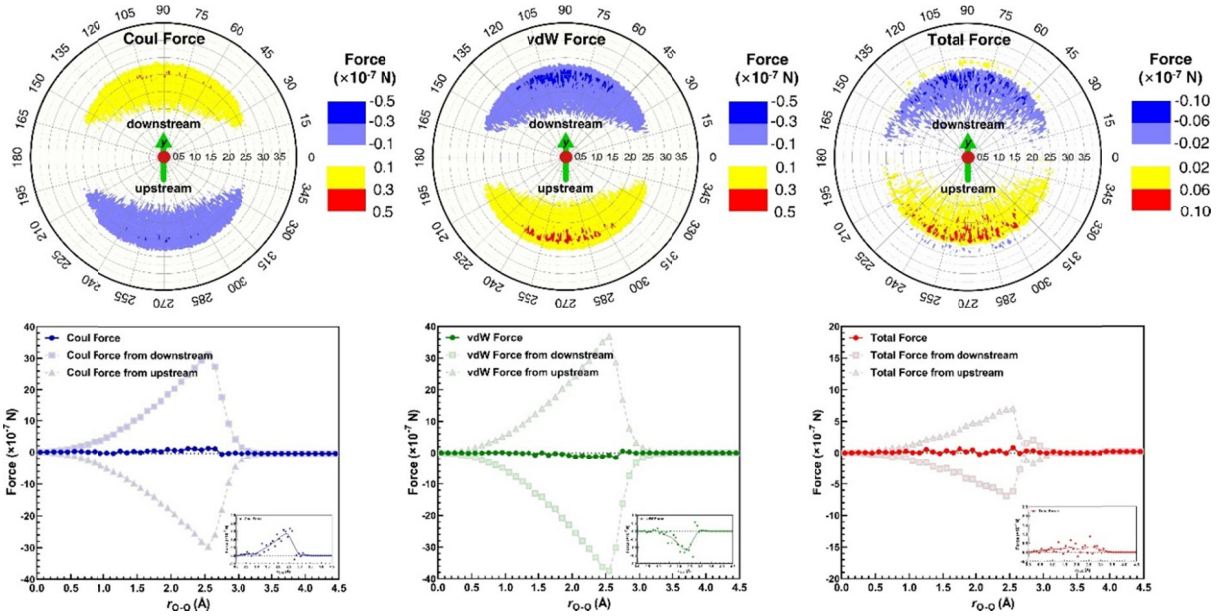

Fig. S12 The planar distribution of forces from water molecules in the FL

REFERENCES

[1] Chen SJ, Chen WQ, Ouyang Y, Matthai S, Zhang L, 2019. Transitions between Nanomechanical and Continuum Mechanical Contacts: New Insights from Liquid Structure. *Nanoscale*, 11, 22954-22963. https://doi.org/10.1039/c9nr07180f

[2] Kondratyuk N, 2019. Contributions of Force Field Interaction Forms to Green-Kubo Viscosity Integral in *n*-alkane Case. *The Journal of Chemical Physics*, 151, 074502. https://doi.org/10.1063/1.5103265

[3] Marry V, Rotenberg B, Turq P, 2008. Structure and Dynamics of Water at a Clay Surface from Molecular Dynamics Simulation. *Physical Chemistry Chemical Physics*, 10, 4802-13. https://doi.org/10.1039/b807288d

[4] Tazi S, Boţan A, Salanne M, Marry V, Turq P, Rotenberg B, 2012. Diffusion Coefficient and Shear Viscosity of Rigid Water Models. *Journal of Physics: Condensed Matter*, 24, 284117. https://doi.org/10.1088/0953-8984/24/28/284117